The Astrophysical Journal, 985:155 (7pp), 2025 June 1 https://doi.org/10.3847/1538-4357/adcf99

Simulation Study of Optical Band Radiation during the Afterglow Phase of Gamma-Ray Bursts Based on the HADAR Experiment

Heng-Jiao Liu[1], Tian-Lu Chen[1], Yi-Qing Guo[2,3,4], Zi-Hao Zhang[1], Yu-Hua Yao[5], Cheng Liu[2], Qing-Yuan Hou[1], Qing-Qian Zhou[1], Mao-Yuan Liu[1], Qi Gao[1], Xiang-Li Qian[6], Jia-Dan Xie[1], Shan-Jie Shu[1], Yuan-Qi Liu[1], Wei-Qi Han[1], Shao-Hua Zhang[1], Ya-Nan Wang[1], Qi-Jiao Fang[1], Zhi-Qiang Zhu[1], Bao-Zhen Liu[1], and You-Liang Feng[1]
[1] The Key Laboratory of Cosmic Rays (Xizang University), Ministry of Education, Lhasa 850000, Tibet, People's Republic of China; chentl@utibet.edu.cn, fengyouliang@utibet.edu.cn
[2] Key Laboratory of Particle Astrophysics, Institute of High Energy Physics, Chinese Academy of Sciences, Beijing 100049, People's Republic of China; guoyq@ihep.ac.cn
[3] University of Chinese Academy of Sciences, 19 A Yuquan Road, Shijingshan District, Beijing 100049, People's Republic of China
[4] TIANFU Cosmic Ray Research Center, Chengdu 610000, People's Republic of China
[5] Wisconsin IceCube Particle Astrophysics Center, University of Wisconsin-Madison, Madison, WI 53703, USA
[6] School of Intelligent Engineering, Shandong Management University, Jinan 250357, People's Republic of China
Received 2024 December 30; revised 2025 April 15; accepted 2025 April 21; published 2025 May 21

Abstract

Studying the afterglow of gamma-ray bursts (GRBs) is essential for refining theoretical models, uncovering their underlying physical processes, and exploring potential new physics. Multiwavelength investigations have emerged as a fundamental approach for deciphering the complex nature of GRBs, harnessing the complementary observational capabilities of advanced spaceborne observatories and sophisticated ground-based facilities. The High Altitude Detection of Astronomical Radiation (HADAR) experiment utilizes a novel wide-angle atmospheric Cherenkov detection technology, offering the advantages of a wide field of view and a low energy threshold. It is capable of not only observing the very-high-energy (VHE) gamma radiation from GRBs but also conducting observational studies on the optical afterglow of GRBs. In this work, we simulated the expected observations of HADAR for the optical and VHE gamma radiation afterglow of GRB 190114C. The results indicate that HADAR can effectively observe both bands of this GRB, particularly demonstrating excellent sensitivity in the optical band and providing good imaging of its radiation process. This demonstrates that HADAR is capable of conducting effective observations and research on the optical radiation of similar GRBs. Its contributions can refine relevant theoretical research and may enable attempts to observe gravitational-wave counterparts.

Unified Astronomy Thesaurus concepts: Gamma-ray bursts (629)

1. Introduction

Gamma-ray bursts (GRBs) are phenomena characterized by a sudden and significant increase in gamma-ray flux from space, representing one of the brightest explosive events known in the Universe (M. Xu & Y.-f. Huang 2012; J. Yang et al. 2022). They are typically produced by the collapse of massive stars at the end of their lifetimes or when two compact stars merge (A. Levan et al. 2016; E. Troja et al. 2022; G. Finneran et al. 2025). Such events result in the formation of an extreme celestial object at the center, which drives a pair of jets moving in opposite directions at speeds close to the speed of light (referred to as relativistic jets; F. M. Rieger & P. Duffy 2005; A. Janiuk & K. Sapountzis 2018). The collision of fast and slow shells within the jets, or the magnetic reconnection and turbulent dissipation within the shells, can both produce instantaneous radiation (M. Arimoto et al. 2024; S. k. M. Rahaman et al. 2024). When the jets sweep through the interstellar medium, the resulting external shock produces afterglow radiation (L.-L. Zhang et al. 2024).

The afterglow radiation of GRBs is detected over a very broad range, including radio (P. Mészáros & M. Rees 1997), millimeter (S. Pandey et al. 2004), infrared (N. Masetti et al. 2003), optical (N. Masetti et al. 2003), ultraviolet (P. W. Roming et al. 2017), X-ray (R. Sari et al. 1998), and gamma-ray bands (H. Abdalla et al. 2021). Research on light curves of early optical afterglows is of significant scientific importance. It aids in understanding the origins of internal and external shocks in GRBs, the properties of jets, the medium environment, and the radiation processes (W. T. Vestrand et al. 2006; N. Fraija et al. 2016; D. Miceli & L. Nava 2022). Through high-precision analysis of light curves, it is possible to reveal the dynamic evolution process of internal shocks within the high-energy radiation regions and the specific mechanisms of external shocks interacting with the surrounding medium. These studies not only help to decipher the energy release and particle acceleration processes inside GRBs but also provide detailed information about the jet structure, dynamical characteristics, and their changes over time. Additionally, early observations of optical afterglow can help scientists determine the environmental conditions of GRB occurrences, such as dense or sparse interstellar medium, thereby providing a more comprehensive understanding of the triggering mechanisms and propagation processes of GRBs. For example, the analysis and study of GRB 221009A have demonstrated the importance of such data (M. Fulton et al. 2023). In-depth research on optical afterglow radiation mechanisms, such as synchrotron radiation (K. C. Cramer 2020) and inverse Compton scattering

(K. Bornikov et al. 2023), not only provides theoretical foundations for other phenomena in high-energy astrophysics but also drives the improvement and development of related physical models.

The first optical and X-ray afterglows were discovered for GRB 970228, confirming the "multiwavelength" nature of afterglows as predicted by the synchrotron/synchrotron self-Compton scattering (SSC) external shock model (P. Mészáros & M. Rees 1997; R. Sari 1998; C. D. Dermer et al. 2000; R. Sari & A. A. Esin 2001; B. Zhang & P. Mészáros 2001). Since then, extensive multiwavelength observations have been conducted for numerous GRBs. In about 37% of cases, GRBs are accompanied by an optical afterglow (J. Greiner 2025). Regular optical afterglow light curves typically exhibit a single power-law decay. However, some GRBs with high-quality data display more complex behaviors, revealing richer features such as early optical flashes (likely originating from an external reverse shock), shallow decay phases (or plateaus), and optical flares or bumps superimposed on the standard afterglow component (L. Li et al. 2012). Additional observational data would be invaluable for studying these features in greater depth among GRBs. The fraction of optically dark GRBs depends on the observational epoch and the sensitivity of the telescopes (B. Zhang 2019). Given the importance of such observations, we have conducted a series of research analyses on the optical afterglow phase of GRBs by leveraging the wide field-of-view and low energy threshold characteristics of the High Altitude Detection of Astronomical Radiation (HADAR) experiment. Moreover, we have utilized the high conversion efficiency of its camera module, which consists of photomultiplier tubes (PMTs) and exhibits high sensitivity to blue and ultraviolet light. These features enable the HADAR experiment to capture the early optical signals of GRBs more quickly and sensitively, providing crucial data support for uncovering the physical mechanisms of GRBs.

The main purpose of this paper is to present observational expectations for the optical band of GRB afterglows and to simultaneously expect the very-high-energy (VHE) observations of GRBs, highlighting the observational advantages of HADAR in both bands. Section 2 introduces the HADAR experiment. Section 3 describes the analysis methods. Section 4 presents the simulation results for the VHE and optical afterglow observations of GRB 190114C. In Section 5, a relevant discussion on the theoretical model was conducted, and the summary is presented in Section 6.

2. HADAR Experiment

The HADAR project is planned to be built at the Yangbajing International Cosmic Ray Observatory (elevation 4300 m, 90.°522E, 30.°102N). The array will consist of four wide-angle atmospheric imaging Cherenkov telescopes, each located at the four corners of a 100 m square. Each telescope comprises a 5 m diameter hemispherical lens, a 7 m tall cylindrical metal container, and a camera module at the bottom. The design of the hemispherical lens allows parallel light rays entering at the edge to focus on the edge of the camera module, achieving a large field of view of $30^\circ \times 30^\circ$. To improve the light transmission, the cylindrical metal container is filled with high-purity water. The camera module, composed of 18,961 densely packed 2 inch PMTs, is placed at the focal plane of the lens and is used for imaging atmospheric Cherenkov light (G.-G. Xin et al. 2022).

In the selection of the camera module, we chose to use PMT instead of the CCD and CMOS commonly used in traditional optical observations. The reason for this is PMT has significant advantages in sensitivity and response speed, making it particularly suitable for capturing rapidly changing weak light signals, such as the optical afterglow of GRBs, which play a crucial role in scientific detection and high-energy physics experiments (Hamamatsu Photonics 2020); CCD performs excellently in high-resolution imaging, suitable for scenarios requiring detailed spectra and high clarity (J. R. Janesick et al. 1987), while CMOS excels in real-time imaging and low-power applications (E. R. Fossum 1997). However, based on the needs of the HADAR experiment, the high sensitivity and fast response of PMT are the characteristics we need more.

HADAR possesses the observational advantages of a wide field of view and low energy threshold. This makes it highly favorable for detecting transient phenomena associated with VHE GRBs (G.-G. Xin et al. 2021; Q.-L. Chen et al. 2023) and facilitates the study of GRBs' optical afterglow radiation, enabling detailed analysis in the optical band.

3. Research Methods

In this section, we will outline the methodology for estimating HADAR's measurement capabilities regarding GRB afterglow emissions. Initially, we will provide a concise description of the simulation of the GRB afterglow emission. Subsequently, leveraging the performance parameters of HADAR, we will conduct a quantitative assessment of its potential for detecting VHE emissions and optical band signals from GRB afterglows.

3.1. GRB Afterglow Radiation

We adopt a forward-shock model centered on a fireball scenario, which is characterized by an impulsive outflow with specific physical parameters: the isotropic-equivalent kinetic energy ($E_{\rm k,iso}$) and the initial Lorentz factor (Γ_0). This relativistic outflow propagates into an external medium of constant number density (n_0). The shock-accelerated electrons follow a power-law energy distribution with index p. These electrons undergo energy loss through two primary mechanisms: (1) synchrotron radiation in the presence of a turbulent magnetic field, and (2) SSC of their self-generated synchrotron photons. The energy partition between electrons and the magnetic field in the shock region is governed by the equipartition parameters $\epsilon_{\rm e}$ and $\epsilon_{\rm B}$, respectively. While the lower energy emission predominantly occurs in the Thomson regime, we incorporate the Klein–Nishina effect in our treatment of the inverse Compton process (X.-Y. Wang et al. 2010). The light curve at a specific observed frequency (ν) can be expressed as a function of the key physical parameters (Y.-H. Yao et al. 2023, 2025; F.-S. Min et al. 2024): $F(t, \nu) = F(t, \nu, E_{\rm k,iso}, \Gamma_0, p, \epsilon_{\rm e}, \epsilon_{\rm B}, n_0)$. For a thorough treatment of the underlying dynamical evolution and radiation mechanisms, we refer the reader to the foundational studies by R. Sari et al. (1998), Y. F. Huang et al. (2000), R. Sari & A. A. Esin (2001), and Y.-Z. Fan et al. (2008). The numerical code employed in this study for modeling GRB afterglow emission was originally developed by R.-Y. Liu et al. (2013) and X.-Y. Wang et al. (2019) and has subsequently been enhanced and implemented in the works of Y.-H. Yao et al. (2023), F.-S. Min et al. (2024), and Y.-H. Yao et al. (2025). In

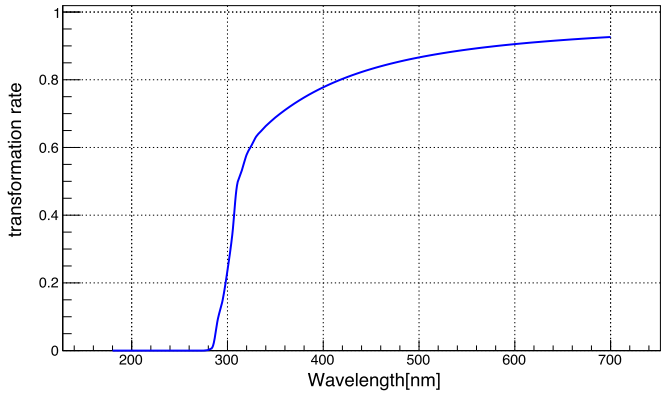

Figure 1. The atmospheric transmission efficiency for photons (180–700 nm) above an altitude of 4300 m, where HADAR is located.

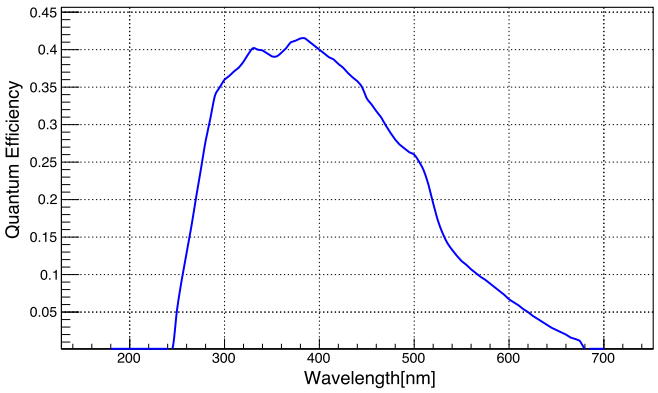

Figure 2. Quantum efficiency of the Hamamatsu R11920 PMT for photons with wavelengths ranging from 180 to 700 nm (S. Eschbach 2019).

the following analysis, we utilize this to simulate the light curves and spectral energy distributions of GRB 190114C as a representative case study. Through these simulations, we demonstrate the capabilities of HADAR in advancing our understanding of GRB afterglow phenomena.

3.2. HADAR's Potential in GRB Afterglow Observations

First, we incorporate the characteristics of HADAR's detectors to consider its observational expectations for the optical band of GRBs afterglow radiation.

Photons propagating through the atmosphere are affected by different attenuation mechanisms depending on their wavelengths: photons below 242 nm are influenced by oxygen dissociation; photons below 290 nm are strongly absorbed by ozone, leading to significant attenuation of ultraviolet light; infrared photons above 800 nm are absorbed by water vapor and carbon dioxide; photons between 290 and 800 nm are primarily affected by Rayleigh scattering and Mie scattering from aerosol particles (K. Ishio 2020; P. Sokolsky & G. Thomson 2020).

HADAR is planned to be constructed at an altitude of 4300 m. In this study, the atmospheric transmission efficiency $at(\lambda)$ for photons was simulated using data from the Central European atmosphere in the CORISKA user manual (K. Bernlöhr 2008), as shown in Figure 1.

At longer wavelengths, the absorption of photons by the atmosphere is significantly reduced, with the majority of absorbed photons concentrated within the range of 180–300 nm.

Both HADAR's lens and the pure water it contains will absorb the photons. The transmittance of the lens to the photon is 90% (A. Bonardi et al. 2014), and the transmittance of pure water to the photon is 89% (H. Cai et al. 2017). The overall transmission rate of both is denoted by α.

HADAR's camera module assembly uses Hamamatsu Model R11920 PMT (S. Eschbach 2019). The quantum efficiency $QE(\lambda)$ of the PMT is shown in Figure 2.

PMTs exhibit high efficiency in converting photons to photoelectrons within the 300–400 nm wavelength range, with a maximum quantum efficiency of 41%.

To further demonstrate HADAR's effectiveness in observing the optical afterglow photons from GRBs, the study analyzed HADAR's sensitivity to these photons:

$$F_{\rm sen}(E_\gamma, t) = F(E_\gamma, t) \times \frac{5}{S}, \tag{1}$$

where $F_{\rm sen}(E_\gamma, t)$ is the flux sensitivity. $F(E_\gamma, t)$ is the flux of the simulated GRBs, calculated by the standard afterglow model (R. Sari et al. 1998) and S is the significance of HADAR's detection of GRBs, which can be calculated using the following formula:

$$S = \frac{N_{\rm op}}{\sqrt{N_{\rm bkg}}}, \tag{2}$$

where $N_{\rm op}$ is the number of signal photoelectrons, which is given by

$$N_{\rm op} = \iiint A \times F(E_\gamma, t) \times at(\lambda) \times \alpha \times QE(\lambda) dE d\lambda dt. \tag{3}$$

A is the effective area calculated based on HADAR's geometric structure, taking into account factors such as mirror refraction, with a value of 72 m^2. The photon wavelength range for the observations is 180–700 nm, corresponding to an energy range of 1–7 eV.

$N_{\rm bkg}$ is the number of background photoelectrons:

$$N_{\rm bkg} = \int {\rm NSB} \times A \times \Omega dt. \tag{4}$$

Night sky background (NSB) is 557(p.e./sr/ns/m^2), which is obtained from the night sky light detector and H.E.S.S. related data, while the solid angle is calculated based on the geometric structure of HADAR itself.

4. Results

GRB 190114C was first detected by the Burst Alert Telescope (BAT) instrument on the Neil Gehrels Swift Observatory (Swift) and the Gamma-Ray Burst Monitor (GBM) instrument on the Fermi satellite at 20:57:03 UTC on 2019 January 14 (marked as T0). It was the first GRB to be observed simultaneously in the high-energy and VHE gamma-ray bands (J. Gropp et al. 2019; R. Hamburg et al. 2019; I. Vovk 2023).

This burst was subsequently detected by several space-based experiments, including Fermi/Large Area Telescope (LAT), INTEGRAL/SPI-ACS, AGILE/MCAL, Insight/HXMT, and Konus-Wind (M. Ravasio et al. 2019; D. Sobczyńska et al.

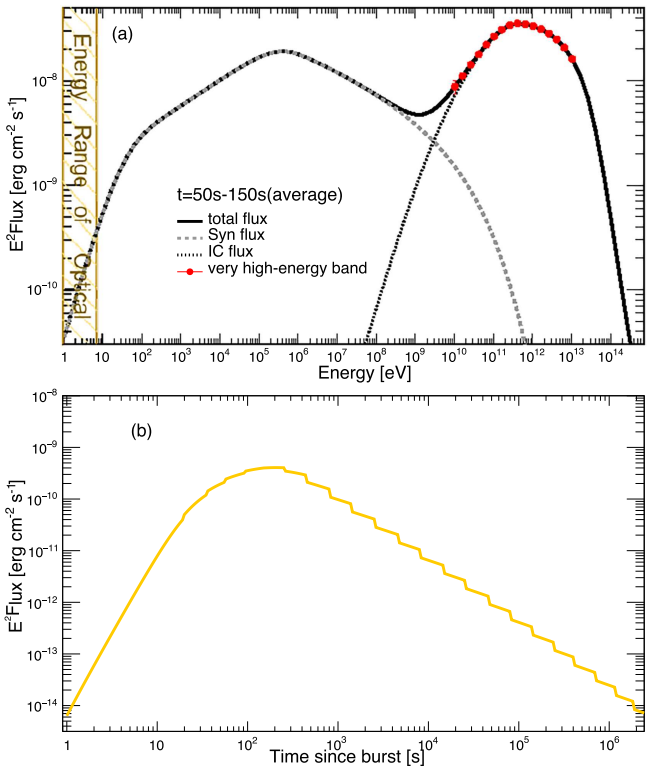

Figure 3. (a) The energy spectrum of GRB 190114C, where the dotted line represents the synchrotron model, the dashed line represents the inverse Compton model, and the solid line represents the combination of both models. The yellow-shaded area indicates the energy range observed by HADAR for the optical afterglow of this GRB (1–7 eV), and the blue star shape with error bars represents the very high-energy observation range (10 GeV–10 TeV). The results show that HADAR also has good observational expectations for the very-high-energy part of this GRB. (b) The light curve of GRB 190114C in the optical band (1–7 eV), based on the model of SSC. The parameters used: isotropic energy $E_k = 6 \times 10^{53}$ erg, initial Lorentz factor $\Gamma_0 = 300$, forward-shock electron energy equipartition factor $\varepsilon_e = 0.07$, forward-shock magnetic field energy equipartition factor $\varepsilon_B = 4 \times 10^{-5}$, electron spectral index $p = 2.5$, density at R_0 $n_0 = 0.3$ cm^{-3}, and redshift $z = 0.4245$ (X.-Y. Wang et al. 2019).

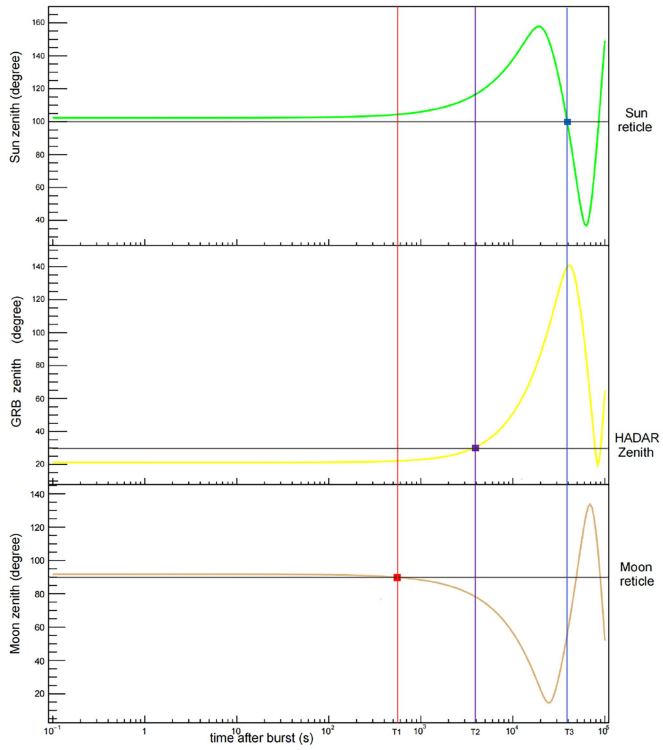

Figure 4. The three panels from top to bottom show the variations of the zenith angles of the Sun, GRB, and the Moon over the time of the GRB 190114C burst, respectively. The gray lines in each panel represent their reference lines. When the Sun and the Moon are below 100° and 90°, respectively, it indicates that they are visible above the horizon, disrupting the clear and moonless night conditions. The reference line for the GRB's zenith angle relative to HADAR's field of view of 30° is marked. When the zenith angle is greater than 30°, the GRB is outside HADAR's field of view. In the panels, the red, purple, and blue vertical lines and squares, respectively, mark the time points when the Moon, the GRB, and the Sun disrupt the observing conditions. The calculations were performed under the assumption of a burst time MJD = 59863.491 for a GRB located at R.A. = 288.°26 and decl. = 9.°8. This was done to determine the tracking of the orbits of GRB, the Moon, and the Sun.

2019). According to measurements by Fermi/GBM, the duration of T90 (i.e., the time interval that contains 90% of the total photon count) was approximately 116 s. However, according to measurements by Swift/BAT, T90 was about 362 s. Additionally, Fermi/GBM observed that the isotropic equivalent energy emitted within the 10–1000 keV energy range during T90 was $E_{\rm iso} \sim 3 \times 10^{53}$ erg, indicating that GRB 190114C also possessed a significant amount of energy in the low-energy band. Moreover, the Major Atmospheric Gamma Imaging Cherenkov (MAGIC) telescopes collaboration conducted detailed observations of the VHE component of GRB 190114C. This observation demonstrates the first clear detection of a GRB in the VHE range by MAGIC. Despite years of searching by MAGIC and other facilities, no definitive VHE gamma-ray detections from GRBs had been achieved prior to this study (D. Sobczyńska et al. 2019). It is evident that GRB 190114C possesses significant observational potential in both the optical and VHE ranges. These characteristics make the analysis and study of this GRB an effective demonstration of the HADAR detector's performance.

According to the methods introduced earlier, the energy spectrum of GRB 190114C (Figure 3(a)) and the light-curve information in the optical band (Figure 3(b)) were analyzed. Using the method of Z.-h. Zhang et al. (2024), as detailed in the Appendix, the spectral observation expectations of HADAR for the VHE phase of this GRB were determined based on the model and effective area. Our findings indicate that the observation error is minimal, yielding accurate and reliable results.

In the actual observation of this GRB, due to the characteristic limitations of the PMTs used in HADAR, observations can only be conducted on clear, moonless nights, and the angle of incidence of the GRB entering HADAR's field of view must be controlled within 30°. Therefore, we conducted a real-time analysis of the zenith angles of the Sun, the Moon, and the GRB sources relative to the horizon and HADAR to determine the effective observation time, as illustrated in Figure 4.

The analysis results indicate that HADAR's effective observation time for GRB 190114C lasted until the Moon rose above the horizon, which is 528 s. During this effective observation time, HADAR further simulated the number of signal photoelectrons and background photoelectrons for this GRB, as shown in Figure 5. The observation's significance was also calculated, as displayed in Figure 6. The results demonstrate that HADAR has an excellent observation effect

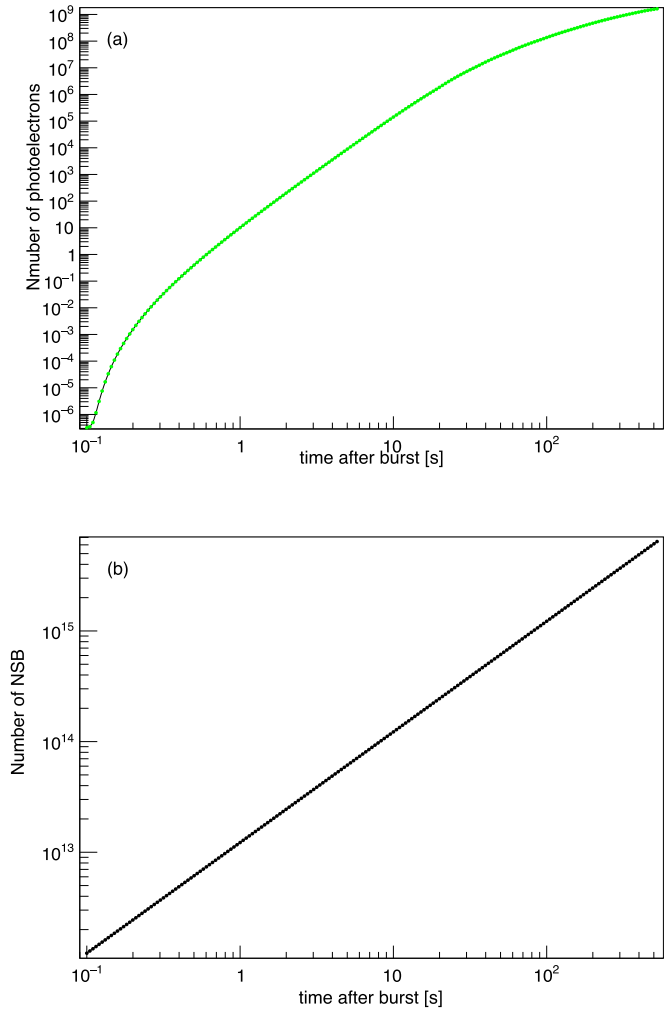

Figure 5. (a) Detection of signal photoelectrons in the optical band of the GRB 190114C afterglow radiation by HADAR over time; (b) detection of background photoelectrons over time. Note that the number of photoelectrons at each time corresponds to the cumulative result within that time period.

on this GRB, with a significance far exceeding the minimum observation expectations.

To comprehensively demonstrate the advantages of HADAR in observations of the optical counterpart of the GRB 190114C afterglow, a simulation analysis of the observational sensitivity for this burst was also conducted. Specifically, it discusses the actual observation results 10 days after the burst, as well as the observation results under ideal conditions within a single night without moonlight. The analysis results are shown in Figure 7.

To evaluate the observation effectiveness, the imaging results of this GRB on the HADAR camera module were also simulated. Using the point-spread function, $g(x, y) = \frac{1}{2\pi\sigma\zeta}\exp[-\frac{(x-x_0)^2}{2\sigma^2} - \frac{(y-y_0)^2}{2\zeta^2}] + b$, we drew the imaging spots under both actual and ideal observation conditions within the first day after the burst, as illustrated in Figure 8.

5. Discussion

During the observation of GRB 130427A, simultaneous optical and VHE observations were conducted, and some theoretical values were compared and discussed in this work. First, E. Aliu et al. (2014), based on VERITAS observations,

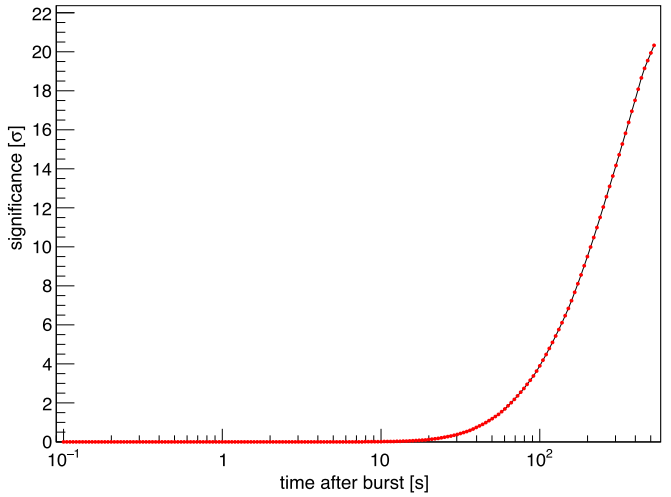

Figure 6. The significance of HADAR's observation of GRB 190114C. Within the effective observation time, the maximum significance is 20.33σ. The significance is calculated based on the data in Figure 5, all within the cumulative time effect.

found limitations in the SSC model for GRB 130427A. The VERITAS upper limits were inconsistent with the SSC models assuming either a spectral break or no break above 120 GeV; only when extrapolating the LAT data based on temporal extrapolation to energies above 100 GeV did the predicted flux conflict with the VERITAS upper limits. This suggests that a simple one-zone SSC model struggles to accurately describe GRB 130427A above 100 GeV, casting doubt on the effectiveness of the SSC mechanism in the high-energy regime. For the SSC explanation to hold, fine-tuning of physical parameters is required, either by having the afterglow dominated by SSC from the initial stages or by achieving a smooth transition from synchrotron-dominated to SSC-dominated emission at later stages. Given these limitations and the complexity of parameter adjustments, the study leans toward a synchrotron radiation explanation for GRB 130427A, indicating that the SSC mechanism has limitations in the high-energy regime. Second, W. T. Vestrand et al. (2014) pointed out that the optical afterglow of GRB 130427A was correlated with the high-energy gamma-ray flux, possibly produced by a reverse shock, and also showed that the optical emission from GRB 130427A was detected for hours after the prompt gamma-ray phase. It is also noteworthy that the optical afterglow emission from GRB 130427A was correlated with the VHE GeV gamma-ray emission. In the case of GRB 190114C discussed in this work, the optical emission was observed during the afterglow phase.

In addition to GRB 190114C, which is discussed in this paper, a growing number of GRBs—including GRB 180720B, GRB 190829A, GRB 201216C, GRB 221009A, as well as GRB 201015A and GRB 160821B—have been reported to emit photons at sub-TeV energies and beyond. Extensive theoretical calculations have been conducted to explain their multi-wavelength observations (G. P. Lamb et al. 2019; O. S. Salafia et al. 2022; LHAASO collaboration 2023; A. K. Ror et al. 2023; Y.-H. Yao et al. 2025), yet a definitive conclusion has yet to be reached. HADAR, with its capability to enhance statistical data, could provide critical insights for further investigations into the VHE physics of GRBs, a field that has also been explored in recent studies (Y.-H. Yao et al. 2023; Z.-h. Zhang et al. 2024).

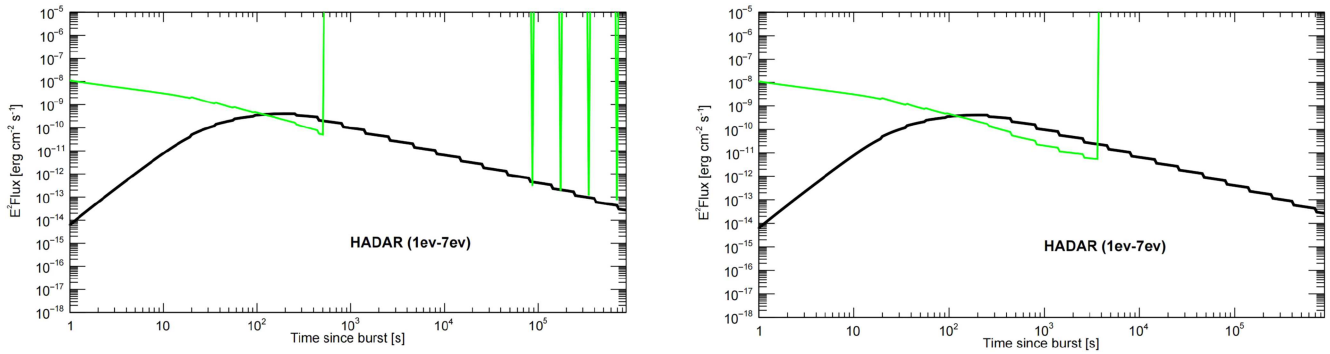

Figure 7. The green line is the sensitivity curve, and the black line is the light curve of GRB 190114C derived from the theoretical model. The left figure shows the observational sensitivity of HADAR under effective observational conditions within 10 days of the GRB 190114C burst. The right figure shows the sensitivity curve changes of HADAR under ideal observational conditions (without the moonlight) within the first day after the burst. The observational time was 3792 s under ideal observational conditions in one day.

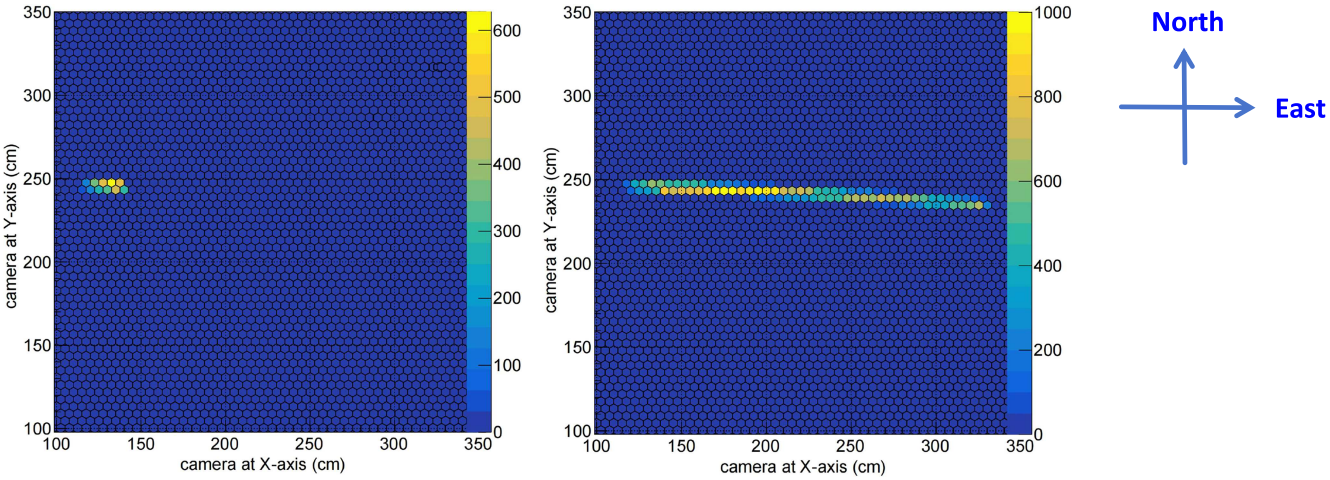

Figure 8. The observation imaging spots of HADAR under actual observation conditions (left) and ideal observation conditions (right) within one day after the GRB 190114C burst. The color scale indicates the amount of charge contained in each PMT, measured in digital counts. The image size refers to the size of the camera module, with the PMTs on the module being 2 inches in size, and the module spans 5 m on both the horizontal and vertical coordinates. The actual observation time was 528 s, while the ideal observation time was 3792 s.

On the other hand, this work also takes optical observations into account, focusing on forward shocks, one of the most widely utilized models in the field. However, some GRBs exhibit additional spectral features, such as flashes, flares, bumps, or other structures superimposed on the standard afterglow optical emission (L. Li et al. 2012). Consequently, the current findings are relatively conservative, as the inclusion of these extra structures and physical processes beyond the forward-shock mechanism would likely increase the number of photons detectable in experiments.

6. Conclusion

The optical band study of GRB afterglow radiation is of great importance for understanding its physical nature, challenging and improving existing theoretical models, exploring new physical phenomena, and studying the evolution of the Universe. Due to the transient and random nature of GRBs, current optical observations face substantial challenges in data acquisition. We fully utilized the high sensitivity and rapid response capabilities of the HADAR experiment to conduct detailed simulation studies and data analyses. The goal was to measure the spectral characteristics and temporal evolution patterns of afterglow radiation more accurately, reveal the shortcomings of existing theoretical models, and promote their further improvement and development.

This paper also analyzes the impact of the atmosphere on photon propagation efficiency and the absorption of photons by telescopes. Additionally, it provides a detailed study of GRB 190114C, including photon detection, significance expectation, sensitivity expectation, and observation trajectory analysis. The study demonstrates that HADAR achieves an observational significance of 20.33σ at 528 s. Under ideal conditions, with an observation duration of 3792 s, the significance increases to 24.58σ at 1380 s, confirming highly reliable observations. Furthermore, the performance of HADAR in sensitivity expectations and observation trajectory analysis demonstrates its significant advantages in optical band photon detection. We also conducted an expectation analysis for the VHE gamma radiation band, and the results reveal that it exhibits good observation expectations. These research findings indicate that HADAR has great observational potential in both the optical band and VHE aspects of gamma GRB afterglow radiation. It is also expected to find electromagnetic counterparts of gravitational waves.

Acknowledgments

This work is supported by the Central Government Funds for Local Scientific and Technological Development (grant No. XZ202301JD0002G), the Natural Science Foundation of Tibet Autonomous Region (grant No. XZ202401ZR0064), the National Natural Science Foundation of China (grant No. 12405128), the National Natural Science Foundation of China (grant No. 12405124), the Central Government Funds for the Reform and Development of Local Colleges and Universities (grant No. 00061082), and High-level Talent Training Program (Xizang University; grant No. 2022-GSP-S049).

Appendix

Considering the need to simulate detector effects, particularly the angular resolution and effective area of HADAR, the simulation process involves generating a large number of extensive air shower samples using the Cosmic Ray Simulations for KASCADE (CORSIKA) program. For the high-energy and low-energy simulations, the QGSJETII-04 and FLUKA models were employed, respectively.

The effective area $S_{\rm eff}[i]$ of the detector in energy range $[i]$ is given by

$$S_{\rm eff}[i] = S_{\rm scatt} \times \frac{N_{\rm cut}[i]}{N_{\rm total}[i]}, \tag{A1}$$

where $S_{\rm scatt}$ is the point area, which is set to $(800 \times 800\,{\rm m}^2)$ in the simulation; $N_{\rm cut}[i]$ represents the number of successful reconstructions; and $N_{\rm total}[i]$ is the total number of simulated instances.

The detector's angular resolution, $\theta[i]$, is defined as the angular difference corresponding to the 68% containment of the distribution of angular differences between reconstructed and true event positions.

The theoretical light curve and theoretical energy spectrum of GRB 190114C were provided by the synchrotron inverse Compton radiation model. Considering that the number of VHE photons $\lambda[i]$ detected by the HADAR detector within a fixed time follows a Poisson distribution, we have

$$P(X = k)[i] = \frac{e^{-\lambda[i]}\lambda[i]^k}{k[i]!}. \tag{A2}$$

The number of VHE photons, $\lambda[i]$, in the range of 50–150 s, can be obtained by integrating the light curve $F_{\rm LC}$:

$$\lambda[i] = \int_{50}^{150} F_{\rm LC} dt \times S_{\rm eff}[i]. \tag{A3}$$

Then, the observational error $e[i]$ for VHE spectra is given by

$$e[i] = \sqrt{\lambda[i]}. \tag{A4}$$

ORCID iDs

Heng-Jiao Liu https://orcid.org/0009-0008-9946-373X
Tian-Lu Chen https://orcid.org/0000-0002-2944-2422
Yi-Qing Guo https://orcid.org/0000-0003-4932-9619

References

Abdalla, H., Aharonian, F., Ait Benkhali, F., et al. 2021, Sci, 372, 1081
Aliu, E., Aune, T., Barnacka, A., et al. 2014, ApJL, 795, L3
Arimoto, M., Asano, K., Kawabata, K. S., et al. 2024, NatAs, 8, 134
Bernlöhr, K. 2008, APh, 30, 149
Bonardi, A., Pühlhofer, G., Hermanutz, S., & Santangelo, A. 2014, ExA, 38, 1
Bornikov, K., Volobuev, I., & Popov, Y. V. 2023, MUPB, 78, 453
Cai, H., Zhang, Y., Liu, C., et al. 2017, JInst, 12, P09023
Chen, Q.-L., Hu, P.-J., Su, J.-J., et al. 2023, ChPhC, 47, 095001
Cramer, K. C. 2020, A Political History of Big Science: The Other Europe (London: Palgrave Macmillan), 59
Dermer, C. D., Chiang, J., & Mitman, K. E. 2000, ApJ, 537, 785
Eschbach, S. 2019, PhD thesis, Friedrich-Alexander-Universitaet Erlangen-Nuernberg
Fan, Y.-Z., Piran, T., Narayan, R., & Wei, D.-M. 2008, MNRAS, 384, 1483
Finneran, G., Cotter, L., & Martin-Carrillo, A. 2025, A&C, 52, 100954
Fossum, E. R. 1997, ITED, 44, 1689
Fraija, N., Lee, W. H., Veres, P., & Duran, R. B. 2016, ApJ, 831, 22
Fulton, M., Smartt, S., Rhodes, L., et al. 2023, ApJL, 946, L22
Greiner, J. 2025, http://www.mpe.mpg.de/~jcg/grbgen.html
Gropp, J., Kennea, J., Klingler, N., et al. 2019, GCN, 23688, 1
Hamamatsu Photonics 2020, Handbook Photomultiplier Tubes Basics and Applications (Hamamatsu: Hamamatsu Photonics) https://psec.uchicago.edu/links/pmt_handbook_complete.pdf
Hamburg, R., Veres, P., Meegan, C., et al. 2019, GCN, 23707, 1
Huang, Y. F., Gou, L. J., Dai, Z. G., & Lu, T. 2000, ApJ, 543, 90
Ishio, K. 2020, PhD thesis, LMU
Janesick, J. R., Elliott, T., Collins, S., Blouke, M. M., & Freeman, J. 1987, OptEn, 26, 692
Janiuk, A., & Sapountzis, K. 2018, in Cosmic Rays, ed. Z. P. Szadkowski (London: IntechOpen),
Lamb, G. P., Tanvir, N., Levan, A., et al. 2019, ApJ, 883, 48
Levan, A., Crowther, P., de Grijs, R., et al. 2016, SSRv, 202, 33
LHAASO collaboration 2023, SciA, 9, eadj2778
Li, L., Liang, E.-W., Tang, Q.-W., et al. 2012, ApJ, 758, 27
Liu, R.-Y., Wang, X.-Y., & Wu, X.-F. 2013, ApJL, 773, L20
Masetti, N., Palazzi, E., Pian, E., et al. 2003, A&A, 404, 465
Mészáros, P., & Rees, M. 1997, ApJ, 476, 232
Miceli, D., & Nava, L. 2022, Galax, 10, 66
Min, F.-S., Yao, Y.-H., Liu, R.-Y., et al. 2024, ApJ, 964, 195
Pandey, S., Sagar, R., Anupama, G., et al. 2004, A&A, 417, 919
Rahaman, S. k. M., Granot, J., & Beniamini, P. 2024, MNRAS: Lett., 528, L45
Ravasio, M., Oganesyan, G., Salafia, O. S., et al. 2019, A&A, 626, A12
Rieger, F. M., & Duffy, P. 2005, ApJL, 632, L21
Roming, P. W., Koch, T. S., Oates, S. R., et al. 2017, ApJS, 228, 13
Ror, A. K., Gupta, R., Jelínek, M., et al. 2023, ApJ, 942, 34
Salafia, O. S., Ravasio, M. E., Yang, J., et al. 2022, ApJL, 931, L19
Sari, R. 1998, ApJL, 494, L49
Sari, R., & Esin, A. A. 2001, ApJ, 548, 787
Sari, R., Piran, T., & Narayan, R. 1998, ApJL, 497, L17
Sobczyńska, D., Bednarek, W., & Sitarek, J. 2019, Natur, 575, 7783
Sokolsky, P., & Thomson, G. 2020, Introduction to Ultrahigh Energy Cosmic Ray Physics (Boca Raton, FL: CRC Press),
Troja, E., Fryer, C., O'Connor, B., et al. 2022, Natur, 612, 228
Vestrand, W. T., Wren, J. A., Panaitescu, A., et al. 2014, Sci, 343, 38
Vestrand, W. T., Wren, J. A., Wozniak, P. R., et al. 2006, Natur, 442, 172
Vovk, I. 2023, PhRvD, 107, 043020
Wang, X.-Y., He, H.-N., Li, Z., Wu, X.-F., & Dai, Z.-G. 2010, ApJ, 712, 1232
Wang, X.-Y., Liu, R.-Y., Zhang, H.-M., Xi, S.-Q., & Zhang, B. 2019, ApJ, 884, 117
Xin, G.-G., Cai, H., Guo, Y.-Q., et al. 2022, NuScT, 33, 25
Xin, G.-G., Yao, Y.-H., Qian, X.-L., et al. 2021, ApJ, 923, 112
Xu, M., & Huang, Y.-f. 2012, PABei, 30, 17
Yang, J., Ai, S., Zhang, B.-B., et al. 2022, Natur, 612, 232
Yao, Y.-H., Min, F.-S., Chen, S., & Guo, Y.-Q. 2025, RAA, 25, 025001
Yao, Y.-H., Wang, Z., Chen, S., et al. 2023, ApJ, 958, 87
Zhang, B. 2019, The Physics of Gamma-ray Bursts (Cambridge: Cambridge Univ. Press),
Zhang, B., & Mészáros, P. 2001, ApJ, 559, 110
Zhang, L.-L., Zhong, S.-Q., Xin, L.-P., & Liang, E.-W. 2024, ApJ, 972, 170
Zhang, Z.-h., Chen, T.-L., Feng, Y.-L., et al. 2024, ApJ, 967, 31